

## Diffusion in Channeled Structures. II. Systems with Large Energy Barriers<sup>†</sup>

Benoit Palmieri and David Ronis\*

Department of Chemistry, McGill University, 801 Sherbrooke Ouest, Montréal, Québec, Canada H3A 2K6

Received: April 29, 2005; In Final Form: June 21, 2005

The methods developed in a previous paper (*Phys. Rev. E: Stat. Phys., Plasmas, Fluids, Relat. Interdiscip. Top.* **2003**, 68, 046127) are used to calculate the permeability of argon in  $\alpha$ -quartz, a system containing large energy barriers. The permeability is reported at three different temperatures and follows Arrhenius behavior. The permeabilities obtained from a hopping model combined with transition state theory closely follow our predicted values but are systematically lower. Lattice flexibility cannot be neglected in this system, and the energy-transfer between  $\alpha$ -quartz and the argon atom through lattice vibrations occurs on a fast enough time scale such that it plays a role in the guest diffusive motion.

### I. Introduction

In a previous paper,<sup>1</sup> henceforth referred to as I, we formulated a theory for calculating the permeability of guest molecules in channeled crystals and applied it to the diffusion of xenon through the zeolite theta-1. The energy landscape inside the theta-1 crystal channels had relatively small energy barriers. In this paper, we will apply the methodology described in I to a system where the energy barriers are large.

In the general approach that we use, based on the work of Ronis and Versteinstein,<sup>2</sup> equations of motion for Gibbs surface excess quantities describing the dynamics in the energy barrier regions were derived using a multipole expansion, first formulated by Ronis and co-workers for a system with one interface.<sup>3</sup> Specifically, if one starts from a generalized diffusion equation that is nonlocal in space, for example, as given by linear response theory, the multipole expansion results in time-correlation function expressions for the parameters appearing in macroscopic boundary conditions and, in particular, gives one for the permeability. This approach allows us to predict the macroscopic permeability that governs the diffusion (in the linear regime) through a crystalline interface from a microscopic evaluation of various correlation functions and naturally gives rise to a transition state sampling scheme.

As was mentioned in I, previous simulation studies have used either frozen or dynamic lattices (see, e.g., refs 4–7). The importance of the flexibility and especially of the lattice vibrations was investigated by us in I, by Kopelevich and Chang,<sup>8</sup> and by Suffritti and co-workers.<sup>9–11</sup> We include the lattice vibrations, as if the crystal was infinite, through a set of exact generalized Langevin equations that describe the motion of selected crystal atoms. Energy transfer between the lattice and the diffusing particle is then included in the simulations. We found in I, for a small energy barrier system, that the energy exchange took place on a relatively long time scale, and the vibrations only had small effects on the diffusive dynamics. In this work, we show how this changes when the coupling to the lattice is stronger, as happens in higher barrier systems.

A more common approach that is used to study intracrystalline diffusion is transition state theory (TST). When the diffusion

is described by a hopping model, TST predicts the values of the rate constants describing the hops. In I, we found that, although the permeability that TST predicted was in the right range, its underlying assumptions were not justified. Here, we will also calculate the permeability using TST and we will see how accurately it describes the diffusion process for a large energy barrier system.

The paper is divided as follows. In section II, we summarize the theory that leads to an expression for the macroscopic permeability and we briefly describe how the necessary microscopic correlation functions were simulated. In section III, we describe the large energy barrier system that we will study and we report the calculated permeabilities at different temperatures. In section IV, the permeabilities are calculated using TST and compared with our predictions. In section V, we relate and compare the permeability with the diffusion coefficient that is measured experimentally, and finally, in section VI, we discuss the role of lattice vibrations for the diffusion in this system and we make some concluding remarks.

### II. Theory

The techniques that we will use in this paper have been described extensively in I or in previous work.<sup>2</sup> Here, we will, therefore, briefly state the governing equations that describe our system and simulation procedure.

First, recall that we are looking at a system where an interface separates two regions of a guest component with different chemical potentials. This interface has a macroscopic thickness,  $2d$ , and is made of a porous crystalline material, idealized here as an aligned single crystal. The steady-state flux,  $j$ , through this material is then characterized by the following equation:

$$j = -P'[\mu(d) - \mu(-d)] \quad (2.1)$$

where  $\mu(\pm d)$  are the chemical potentials at the interface boundaries and  $P'$  is the permeability intrinsic to the material and is given by

$$\frac{1}{P'} = \frac{1}{\beta} \int_{-d}^d dz \frac{1}{D(z)} \quad (2.2)$$

where  $\beta \equiv 1/k_B T$ ,  $T$  is the temperature, and  $D(z)$  is a space-

<sup>†</sup> Part of the special issue "Irwin Oppenheim Festschrift".

\* To whom correspondence should be addressed. E-mail: David.Ronis@McGill.ca.

-dependent Onsager diffusion coefficient given by

$$D(z) = \frac{1}{A} \int_0^\infty dt \int d\mathbf{r}_\parallel \int d\mathbf{r}' \langle \mathbf{J}_z^\dagger(\mathbf{r}, t) \mathbf{J}_z^\dagger(\mathbf{r}') \rangle \quad (2.3)$$

where  $\mathbf{J}_z^\dagger$  is the  $z$  component of the irreversible or dissipative part of the current and  $A$  is the area of the crystal. Also note that the integration variable,  $z$ , is defined to be normal to the interface (i.e., parallel to the net flux) and is perpendicular to  $\mathbf{r}_\parallel$ .

The time correlation function that appears in eq 2.3 is not directly amenable to simulation since the dynamics in  $\mathbf{J}_z^\dagger(\mathbf{r}, t)$  include a projection operator that projects out the slow parts of the motion (in practice, the parts not included explicitly in the macroscopic equations).<sup>12</sup> By manipulating the well-known integral equations relating correlation and memory functions, Vertenstein and Ronis<sup>2,12</sup> obtained an approximate expression for  $D(z)$  by assuming infinite dilution inside the material and that  $D(z) e^{\beta W(z)}$  is approximately constant near the  $W(z)$  barrier tops; the result is that

$$D(z) = \frac{n_\infty \int_0^\infty dt_1 \int d\mathbf{r}_\parallel \langle v_z(t_1) v_z \rangle_{\mathbf{r}} e^{-\beta W(\mathbf{r})}}{A + \int_0^\infty dt_1 \int d\mathbf{r}_\parallel \langle \beta F[z(t_1)] v_z \rangle_{\mathbf{r}} e^{-\beta [W(\mathbf{r}) - W(z)]}} \quad (2.4)$$

where  $n_\infty$  is the number density of the guest in the bulk,  $v_z$  is the  $z$  component of the guest velocity,  $\langle \dots \rangle_{\mathbf{r}}$  denotes a conditional equilibrium average under the constraint that the initial position of the guest is  $\mathbf{r}$ , and  $W(z)$  and  $F(z)$  are the plane averaged potential of mean force and mean force of the guest in the plane  $z$ , respectively (we distinguish the plane average quantities and their 3D counterparts by the argument to the function,  $z$  in the former and  $\mathbf{r}$  in the latter); in particular,

$$e^{-\beta W(z)} \equiv A^{-1} \int d\mathbf{r}_\parallel e^{-\beta W(\mathbf{r})}$$

Note that the denominator in eq 2.4 approximately reproduces the effect of the projection operator that is implicit in  $\mathbf{J}^\dagger$ , the irreversible part of the current, compare to eq 2.3.

It follows from eqs 2.3 or 2.4 that  $D(z)$  will be small when  $z$  is a barrier-top plane, and it is just these planes that give the main contributions to the permeability, compare to eq 2.2. Hence, provided that a practical way is found for calculating the potential of mean force near the transition states (e.g., analytically or using umbrella sampling), our theory becomes a transition state sampling method, only requiring a knowledge of dynamical correlations for initial states near the transition state.

Clearly, it is necessary to simulate the guest dynamics inside the crystal in order to calculate the time correlation functions appearing in eq 2.4. As described in I, we assume that the guest interacts with a limited number of crystal atoms (referred to as the “target atoms”, or  $T$  for short). The effect of the rest of the crystal (the bath) will be described using a projection operator approach,<sup>13</sup> where the projection operator is an average over the bath degrees of freedom and gives rise to the following generalized Langevin equation:

$$\frac{d\mathbf{p}(t)}{dt} = -\frac{dU[\mathbf{r}(t), R_T(t)]}{d\mathbf{r}} \quad (2.5)$$

and

$$\begin{aligned} \frac{dP_T(t)}{dt} = & -K_{\text{eff}} R_T(t) - \frac{dU[\mathbf{r}(t), R_T(t)]}{dR_T} + \\ & F_T^\dagger(t) - \beta \int_0^t d\tau \langle F_T^\dagger(t - \tau) (F_T^\dagger)^\top \rangle \dot{R}_T(\tau) \end{aligned} \quad (2.6)$$

where  $U$  is the potential interaction between the guest and the target atoms,  $R_T$  and  $P_T$  are, respectively, the target position and momentum column vectors,  $K_{\text{eff}}$  is an effective force constant matrix,  $F_T^\dagger$  is a colored Gaussian noise column vector with zero mean and variance matrix  $\langle F_T^\dagger(t) (F_T^\dagger)^\top \rangle$ , and the  $T$  superscript indicates a transpose.

The projection operator drops out of the time dependence of the memory function, which is obtained by considering the harmonic motion of the bath in the presence of frozen target and guest. Note that these equations are exact, provided that the interaction between the crystal atoms is harmonic and provided that the guest does not directly interact with the bath (this last point can be relaxed somewhat to allow for direct harmonic interactions between the guest and the bath). In I, we described, in detail, the procedures that allow us to calculate  $K_{\text{eff}}$  and  $\beta \langle F_T^\dagger(t) (F_T^\dagger)^\top \rangle$ . When the Laplace transform of the memory function is approximately written as

$$\beta \langle F_T^\dagger(s) (F_T^\dagger)^\top \rangle = \frac{s}{A + B \cdot s + C \cdot s^2} \quad (2.7)$$

the equations of motions simplify to a set of coupled stochastic differential equations with additive white noise, which, by properly choosing the matrices  $A$ ,  $B$ , and  $C$ , reproduces the basic features of the infinite crystal vibrational density of states (cf. I and Figure 1).

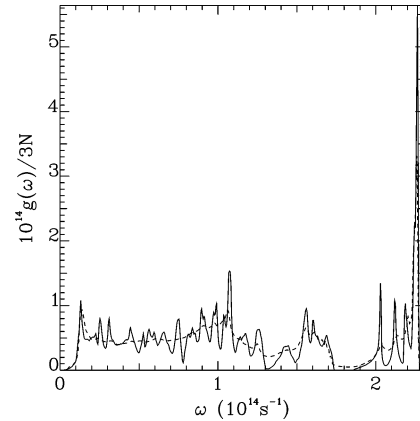


**Figure 1.** Exact density of states (full line) for  $\alpha$ -quartz obtained from a Brillouin zone calculation compared with the approximate density of states (dashed line) that is reproduced from eq 2.7.

Finally, a low-temperature expansion for the potential of mean force was developed and to linear order in  $T$  gives

$$\begin{aligned} W(\mathbf{r}) = & U(\mathbf{r}, R_T^{(0)}) + \\ & \frac{1}{2} R_T^{(0)\top} K_{\text{eff}} R_T^{(0)} + \frac{k_B T}{2} \ln \left\{ \det \left[ 1 + K_{\text{eff}}^{-1} \frac{\partial^2 U(\mathbf{r}, R_T^{(0)})}{\partial R_T^2} \right] \right\} \end{aligned} \quad (2.8)$$

where

$$K_{\text{eff}} R_T^{(0)} = -\frac{\partial U(\mathbf{r}, R_T^{(0)})}{\partial R_T} \quad (2.9)$$

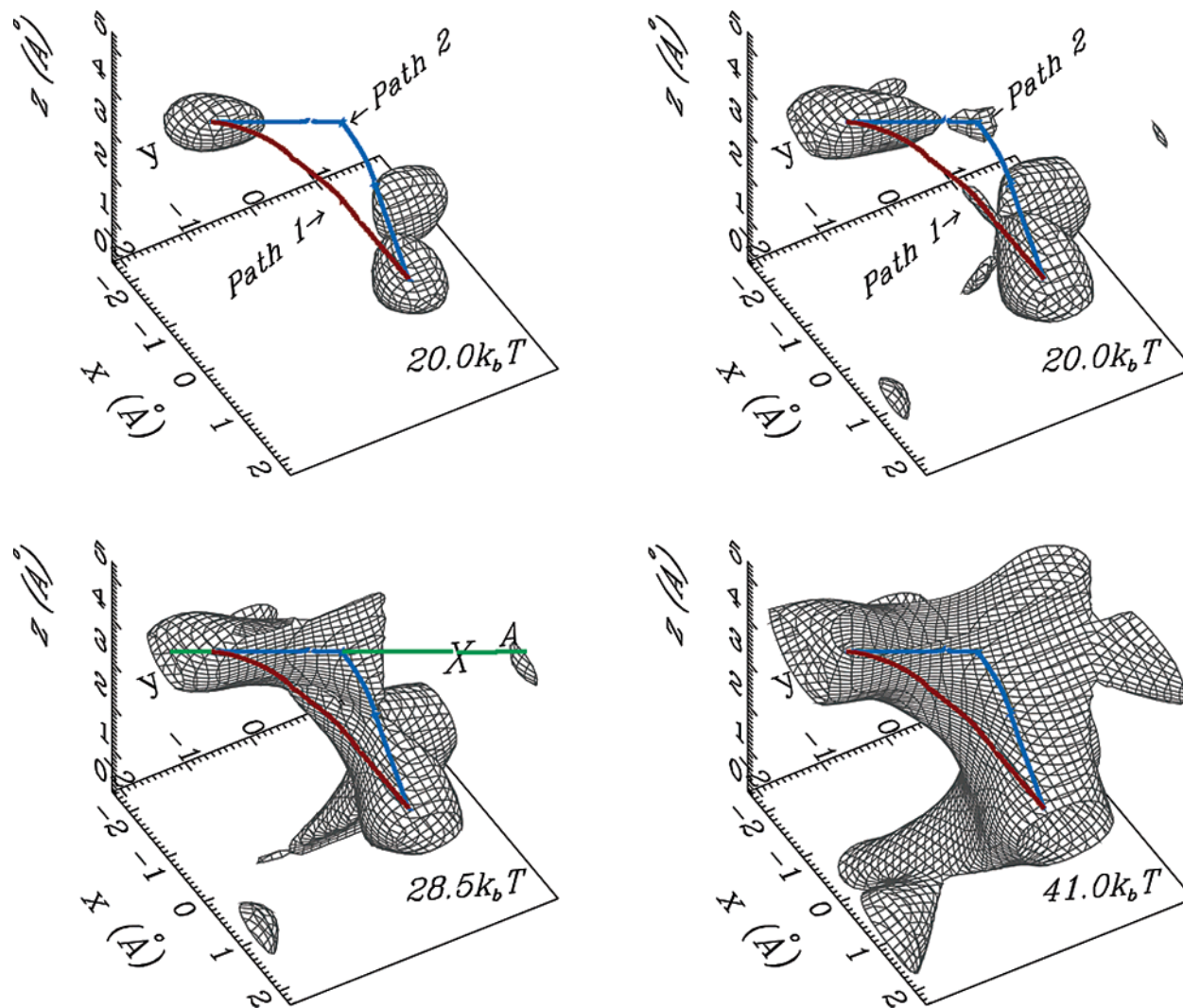


**Figure 2.** Constant potential of mean force surfaces for argon in  $\alpha$ -quartz at 300 K. The surface energy is indicated in the corner of each subfigure. Two symmetry-equivalent low-energy reaction coordinates are shown as paths 1 (red) and 2 (blue). The kink is the position of a local minimum along the path. Also shown is a high-energy reaction coordinate (green) connecting different channels in different unit cells (the saddle point is indicated by an "X").

defines new equilibrium lattice positions,  $R_T^{(0)}$ , where the net force on the target atoms is zero in the presence of a guest fixed at  $\mathbf{r}$ .

### III. Results

**A. Specification of the System.** The system that we will be working with is argon diffusing in  $\alpha$ -quartz. This crystal contains multidimensional interconnected channels that are roughly the size of an argon atom (3–4 Å). Note that quartz shows a phase transition from the  $\alpha$  to the  $\beta$  structures at 846 K;<sup>14</sup> hence, we will work below this temperature. The coordinates of the nine crystal atoms in the unit cell were obtained from ref 15. The interatomic crystal potential, which we describe solely by stretches and bends, is described in I. The vibrational density of states obtained from our model is shown in Figure 1, and it agrees well with other calculations.<sup>16</sup> Our target zone is centered at a corner of the primitive unit cell and is rectangular with dimensions (14.7402, 14.7402, 16.2156 Å). It contains 279 atoms and is large enough such that the interaction energy between the guest and bath is small.

In I, the target-guest interactions were described in terms of a Lennard-Jones potential and lattice partial-charge guest polarization interactions. Here, we use the Lennard-Jones term

only, with parameters that differ slightly from I (cf. section V). We have tested our approximate expression for the potential of mean force, eq 2.8, by comparing the resulting mean force against the numerically simulated average force on a frozen guest after the lattice has equilibrated. The agreement was excellent for the three temperatures we will consider, namely, 100, 300, and, surprisingly, even at 800 K (remember that eq 2.8 is a low-temperature expansion).

Some constant potential of mean force surfaces are shown in Figure 2 at 300 K. The three binding sites in the unit cell are equally separated along the  $z$  axis in a spiral staircase conformation. Each pair of nearest-neighbor binding sites is connected by two symmetry-related steepest descent paths. They go through a local minimum and have two saddle points along the way (see the  $25.7k_B T$  contour of Figures 2, and Figure 3 which shows the potential of mean force along the path). The guest, at least at 300 K, will preferably travel along reaction paths 1 and 2, shown in Figure 2, and will undergo a net displacement along  $z$ . From Figure 2 at  $28.5k_B T$ , we see that the channels lie along  $z$  and are disconnected at moderate energies. To travel from one channel to another, the guest must overcome a larger barrier. This is seen from the dashed line in Figure 3 and by the pocket labeled "A" in Figure 2 that makes a connection

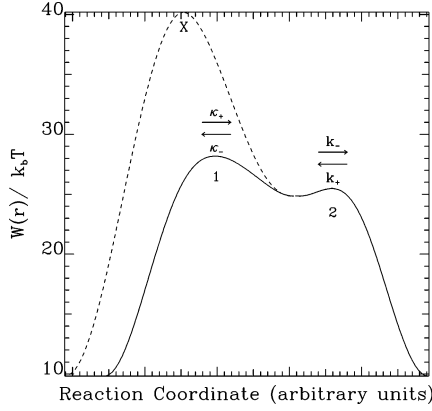


**Figure 3.** Potential of mean force along the reaction coordinate (Paths 1 and 2 in Figure 2), shown as the full line. The dashed line shows the potential of mean force for a reaction coordinate that connects different channels, compare to Figure 2. The saddle point at “X” is indicated in Figure 2. The rate constants used in TST, compare to eq 4.1, are also indicated at the two saddle points 1 and 2.

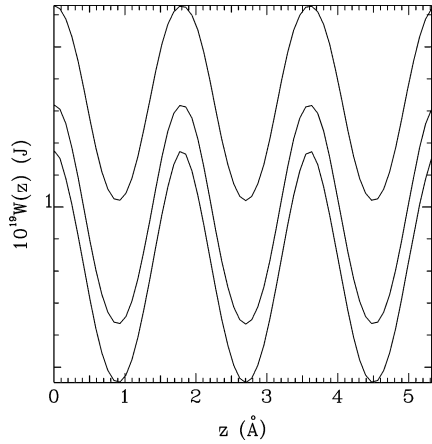


**Figure 4.** Plane average potential of mean force. The temperatures are, starting with the bottom curve,  $T = 100, 300$ , and  $800$  K.

with the channel only at  $41.0k_B T$ . Hence, the channels will behave as if they are disconnected, at least at 100 and 300 K. Also shown in Figure 2 is the high energy reaction coordinate that connects neighboring channels and whose saddle point is indicated by an “X”.

The plane average potentials of mean force,  $W(z)$ , at the temperatures of interest are shown in Figure 4. Note the significant increase with temperature in the absolute potential of mean force, a feature we did not observe in I. On the other hand, the activation energy, obtained from  $W(z)$ , for the individual hops between the binding sites, decreases, albeit very slightly, with an increase in temperature.

**B. Permeabilities.** The first step in calculating the permeabilities,  $P'$ , is to obtain the time-correlations functions appearing in eq 2.4. This was done by simulating eqs 2.5 and 2.6 with a second-order stochastic Runge–Kutta integrator.<sup>17</sup> The required correlation functions at any initial guest position were obtained from an ensemble average of 2000 trajectories. Each of the trajectories was “aged”, keeping the guest frozen while the lattice equilibrated. The aging and running times for the individual runs were  $4.096 \times 10^{-12}$  s. The simulations and ensemble averaging were performed on a Beowulf Cluster containing 64 processors. The plane averages appearing in eq 2.4 were computed using finite grids that contained from 35 to 72 points.

Understanding that  $D(z)$  must scale with the probability of being in the  $z$  plane, which is proportional to  $e^{-\beta W(z)}$ , it is clear

**TABLE 1:  $D_0$  and  $P'$  as a Function of Temperature<sup>a</sup>**

$T$ K	$D_0 \times 10^9$ $m^2 s^{-1}$	$P'/n_\infty e^{\beta W_{\text{Bulk}}}$ $s/m \text{ kg}$	$D_{0,\text{TST}} \times 10^9$ $m^2 s^{-1}$	$P'_{\text{TST}}/n_\infty e^{\beta W_{\text{Bulk}}}$ $s/m \text{ kg}$
100	0.81	$1.17 \times 10^{-24}$	0.05	$2.46 \times 10^{-25}$
300	3.46	$9.76 \times 10^{-2}$	0.21	$2.95 \times 10^{-2}$
800	8.69	$1.20 \times 10^6$	0.71	$5.49 \times 10^5$

<sup>a</sup>  $P'_{\text{TST}}$  and  $D_{0,\text{TST}}$  are the values obtained from TST.

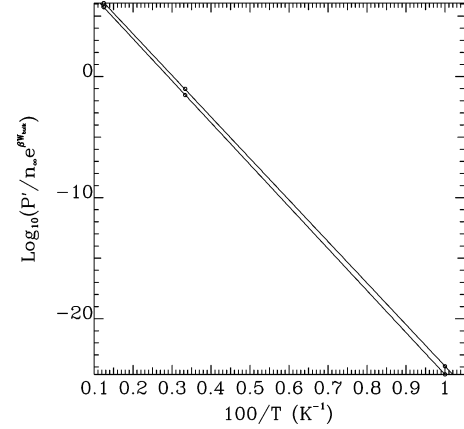


**Figure 5.** Intrinsic permeability,  $P'$ , showing Arrhenius behavior in the temperature range, 100–800 K. The top line shows  $\ln(P'/n_\infty e^{\beta W_{\text{Bulk}}})$ , while the bottom line shows  $\ln(P'_{\text{TST}}/n_\infty e^{\beta W_{\text{Bulk}}})$ .

from eq 2.2 that the main contribution to the permeability will come from the planes where  $W(z)$  is large. We have checked numerically that  $D(z) = n_\infty D_0(T) e^{-\beta W(z)}$  is approximately true near the barrier tops, and the proportionality constant,  $D_0(T)$ , is reported in Table 1. In the same table, we report the values of  $P'/n_\infty e^{\beta W_{\text{Bulk}}}$  at the three temperatures. Note that the potential of mean force in the bulk was kept unspecified here. The log of the permeability is shown in Figure 5 as a function of  $1/T$ . This figure shows that the permeability has an Arrhenius form.

#### IV. Transition State Theory

As discussed in I, an easy and much more common way of obtaining an estimate for the permeability is TST. Of the many assumptions involved in TST, a crucial one is that the trajectory of the diffusing particle, on average, follows the reaction coordinate or a steepest descent path that links different binding sites. In I, we showed that this is invalid for small energy barrier systems. We now present the permeabilities for the present system using TST.

In a hopping model that incorporates the two paths shown in Figure 2, and that takes into account the local minima that these paths cross, the steady-state flux through the material is given by

$$j = -\frac{2\kappa_+ K_{\text{eq}} n_\infty}{k_B T N (1 + \kappa_-/k_-)} (\mu_+ - \mu_-) \quad (4.1)$$

where  $\kappa_\pm$  and  $k_\pm$  are the rate constants whose respective rate processes are indicated in Figure 3. The equilibrium constant  $K_{\text{eq}}$  describes the equilibrium between the gas in the bulk and the first layers of binding sites (assuming that their energies are the same as those for sites well inside the crystal). Finally,  $N$  is the number of binding sites in a channel of a given length, here, 3 per unit cell. In obtaining eq 4.1, we have assumed that the gas in the bulk is ideal, hence,  $\delta\beta\mu_\pm \sim \delta n_\pm/n_\infty$ .

TST gives analytical expressions for all rate constants in eq 4.1, while  $K_{\text{eq}}$  can be obtained from a Langmuir adsorption model, which assumes equilibrium between the gas and binding



sites in the outermost layer of the crystal; this gives

$$\kappa_+ K_{\text{eq}} = \left[ \frac{2\pi(k_B T)^3}{m\eta_1^+ \zeta_1^+} \right]^{1/2} \rho_c e^{-\beta(W_1^+ - W_{\text{Bulk}})} \quad (4.2)$$

and

$$\frac{\kappa_-}{k_-} = \left( \frac{\eta_2^+ \zeta_2^+}{\eta_1^+ \zeta_1^+} \right)^{1/2} e^{-\beta(W_1^+ - W_2^+)} \quad (4.3)$$

where  $W_i^+$  is the potential of mean force, while  $\eta_i^+$  and  $\zeta_i^+$  are the two positive potential of mean force curvature eigenvalues at the  $i$ th saddle point,  $\rho_c$  is the channel density per unit area, and  $m$  is the mass of the guest. Note that partition functions for the binding sites drop out of the final expression, compare to eq 4.2. The permeability predicted by TST is obtained from eqs 4.1 and 4.2 and gives

$$\frac{P'_{\text{TST}}}{n_\infty} = 2 \frac{\rho_c \kappa_+ K_{\text{eq}}}{k_B T N (1 + \kappa_- / k_-)} \approx 2 \frac{\rho_c \kappa_+ K_{\text{eq}}}{k_B T N} \quad (4.4)$$

where the last approximation is valid when  $W_1^+ \gg W_2^+$  (this is the case for 100 and 300 K but not for 800 K, and the full expression will be used for the three cases). In this limit, the effective hopping rate constant between two binding sites is unaffected by the local minimum. The permeabilities can now be calculated. They are reported in Table 1 and are plotted in Figure 5 for comparison with the permeabilities using the theory in I. It is seen that the temperature dependence predicted by TST is close to our value, while the actual permeabilities are consistently lower.

## V. Comparison With Experiment

We now compare our results with experimental argon diffusivities obtained by Watson and Cherniak.<sup>18</sup> This group studied the diffusion of argon into  $\alpha$ - and  $\beta$ -quartz. In this study, the silica surface was exposed to pressurized argon (around 100 MPa) for several hours. Then, the near-surface region was analyzed using Rutherford backscattering spectrometry, a technique capable of measuring the concentration profile of various species inside the material.<sup>19</sup> These profiles were fitted to the solution of the 1D diffusion equation

$$\frac{\partial n(z,t)}{\partial t} = D \frac{\partial^2 n(z,t)}{\partial z^2} \quad (5.1)$$

which describes the density  $n(z, t)$  of argon inside the material as a function of time,  $t$ , and depth,  $z$ , to obtain the diffusion coefficient,  $D$ .

The diffusion equation applied to our system under steady-state conditions gives, for the net flux,

$$j = -\frac{D}{2d} [n(d) - n(-d)] \quad (5.2)$$

where, as usual,  $2d$  is the thickness of the crystalline interface and  $n(\pm d)$  is the density at the boundaries. By rewriting the last equation in terms of the difference in chemical potentials, we obtain

$$j = -\frac{D}{2d} \left( \frac{\partial n_\infty}{\partial \mu} \right)_\beta [\mu(d) - \mu(-d)] \quad (5.3)$$

in the linear regime. It is easily shown that the permeability

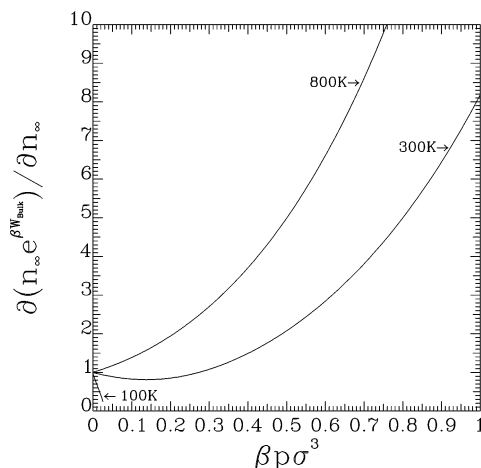


**Figure 6.** Nonideal bulk correction factor appearing in eq 5.4 for a Lennard-Jones fluid with argon-like parameters<sup>20</sup> as a function of pressure,  $p$ , using the HNC approximation and the compressibility relation for the pressure ( $\sigma$  is the Lennard-Jones size parameter). Note that the HNC solution becomes unphysical for pressures beyond those shown in the figure at 100 K, possibly signaling a phase transition.

and the diffusion coefficient are related by

$$D = 2dk_B T \left[ \frac{\partial}{\partial n_\infty} (n_\infty e^{\beta W_{\text{Bulk}}}) \right] \frac{P'}{n_\infty e^{\beta W_{\text{Bulk}}}} \quad (5.4)$$

where  $W_{\text{Bulk}} = \Delta\mu$  is the nonideal part of the guest chemical potential in the bulk. For ideal gases, the factor in square brackets in eq 5.4 is equal to 1, but at the experimental pressures (around 100 MPa), the nonideal corrections are non-negligible. We computed the quantity appearing in the square brackets by numerically solving the hypernetted chain equation (HNC) for a bulk Lennard-Jones fluid and noting that

$$\left( \frac{\partial \beta \Delta\mu}{\partial n} \right)_\beta = -\tilde{c}(\beta, n) \quad (5.5)$$

and

$$\beta p = n - \int_0^n dn \, n \tilde{c}(\beta, n) \quad (5.6)$$

where  $\tilde{c}(\beta, n)$  is the zero wave-vector Fourier transform of the direct correlation function<sup>20</sup> and  $p$  is the pressure. Note that eq 5.6 is the well-known compressibility expression for the equation of state. Finally, we can use the HNC results for  $\tilde{c}(\beta, n)$  to numerically integrate eqs 5.5 and 5.6, and the result is shown in Figure 6.

We are now in position to compare our predicted  $D$  with the experimental ones. The experiment reports the full diffusion coefficient as follows:

$$D = D' e^{-\beta \Delta E^*} \quad (5.7)$$

In terms of TST, the diffusion constant for multiple-barrier channel hops takes the form

$$D = \frac{k_B T}{h} e^{-\beta \Delta A^*} \frac{4d\rho_c (T_0)^{3/2}}{N\rho_0 (T)} \quad (5.8)$$

where  $h$  is Planck's constant and where  $\rho_0$  and  $T_0$  are the bulk gas density and temperature, respectively, in the standard state (here 300 K and 1 atm). The activation free energy is easily obtained by using either our result or TST's result for  $D$ , compare to eq 5.4, in the last equation. The activation Helmholtz

**TABLE 2: Comparison with Experimental Diffusion Coefficients for the Two Potential Models, a and b**

	our method		TST		ref 18 ( $\alpha$ -quartz)
	a	b	a	b	
$\Delta E^\ddagger/k_B(K)$	7863	20 304	7912	20 601	$6150 \pm 750$
$\Delta S^\ddagger/k_B$	-11.80	-13.28	-12.52	-13.72	-32.47
$D_{800}(m^2/s)$	$7.80 \times 10^{-10}$	$1.75 \times 10^{-10}$	$3.80 \times 10^{-10}$	$1.13 \times 10^{-10}$	$8.2^{+8.8}_{-4.2} \times 10^{-19}$
$-\log_{10} D_{800}$	13.38	20.78	13.72	21.13	21.43

free energy takes the usual form,  $\Delta A^\ddagger = \Delta E^\ddagger - T\Delta S^\ddagger$ , where, as usual,  $\Delta E^\ddagger$  is obtained from the slope of a plot of  $\Delta A^\ddagger/T$  versus  $1/T$ , compare to Figure 5. In Table 2, we report  $\Delta E^\ddagger$ ,  $\Delta S^\ddagger$ , and  $D'$  and compare them with the experimental values. We report both calculated and experimental  $D'$  only at 800 K because the experiment never considered room temperature or lower.

The Lennard-Jones parameters that we used are the same as those in I, but with modified target atoms radii ( $r_O = 0.9720 \text{ \AA}$  and  $r_{Si} = 0.6380 \text{ \AA}$ ) such that our  $\Delta E^\ddagger$  agrees well with the experiment. This set of potential parameters, used everywhere unless specified otherwise, is denoted as “a” in Table 2. For this potential, the Arrhenius pre-exponential factor, that is,  $D'_{800}$ , differs by 8 orders of magnitude from that reported by Watson and Cherniak and the overall  $D$  at 800 K also differs by 8 orders of magnitude. Such a big difference very likely arises from a Boltzmann factor and strongly suggests that the current potential parameters (“a”) underestimate the strength of the actual guest–lattice interactions and that the already large energy barriers of the system are, in fact, even larger.

The limited free volume for argon to diffuse in  $\alpha$ -quartz implies that argon is always in regions of strong repulsive potential of the closest crystal atoms. In this regime, small changes in the potentials’ parameters can drastically change the shape of potential surfaces. In fact, the depth of our Lennard-Jones potential was obtained in I from the London formula,<sup>24</sup> and it is well-known that this approach tends to give smaller depths than others (like the Kirkwood–Muller<sup>25,26</sup> formula). In ref 27, it is shown that the London formula can give depths that are too small by a factor of 3. Moreover, these formulas model the attractive part of the potential. Here, it is the repulsive part that would need to be modeled accurately. As a test, we have redone the calculation with an increased well depth (3 times larger), increased oxygens radii (15% larger), and increased force constants (20% larger). While the basic features of the energy landscape are preserved with these parameters, albeit at higher energies, the local minimum separating the binding sites disappears. The results with this potential are denoted as “b” in Table 2. The overall diffusion constant at 800 K agrees well with the experiment, but the  $\Delta E^\ddagger$  is now 3 times too large. For both sets of potential parameters, the factor  $D'_{800}$  is not well reproduced. This indicates that both potentials fail to describe accurately the entropy loss as the lattice rearranges in the presence of the guest.

In I, we noted that our potential model was only qualitative, but since the typical energies were small, the accuracy was reasonable. Here, mainly because the energies are large, small changes in the potential parameters lead to large changes in  $D$ . An accurate potential model would be necessary for good agreement with the experiments. Of the limitations of our potential model are the facts that the repulsive part is poorly described, we have neglected all long-range interactions, and the lattice may start to show anharmonic effects considering the large displacements that are induced by the guest. Note that there are certainly some sources of errors in the experiments coming from surface effects, defects, impurities, and nanochan-

nels, but Watson and Cherniak carefully checked that these were small and, in any event, cannot be used to explain an  $O(10^7)$  difference.

## VI. Discussion

The effect of the crystal vibrations on the guest motion was also addressed in I, where we found that neglecting the lattice vibrations introduced only small errors for a system with small energy barriers. Here, we consider again the role of lattice vibrations. The effect of the crystal motion appears in several ways. First, at the level of the potential of mean force, allowing the lattice to relax to a new equilibrium position in the presence of the guest (cf. eq 2.9) significantly reduces the energy barriers in  $W(z)$ , for example, by  $60k_B T$  at 300 K and  $18k_B T$  at 800 K. As was mentioned before, this happens because the argon atom is always in the steep repulsive part of the closest lattice atoms before they are allowed to relax. Also note that the flexibility of the lattice is responsible for the temperature-dependent part of  $W(r)$ .

Second, aside from mean potentials, the question of the importance of the lattice vibrations on the guest dynamics can be addressed by comparing the velocity autocorrelation functions for an argon atom released from a saddle point in our dynamic lattice and in an adiabatically equilibrated lattice. In the latter case, we mean that the lattice follows the guest adiabatically such that the net force on the lattice remains zero at all times. This is achieved using an initial  $R_T^{(0)}$  that solves eq 2.9 and propagating  $R_T^{(0)}$  in time according to

$$\frac{dR_T^{(0)}}{dt} = - \left[ K_{\text{eff}} + \frac{\partial^2 U(\mathbf{r}, R_T^{(0)})}{\partial R_T^{(0)} \partial R_T^{(0)}} \right]^{-1} \frac{\partial^2 U(\mathbf{r}, R_T^{(0)})}{\partial R_T^{(0)} \partial \mathbf{r}} \frac{d\mathbf{r}}{dt} \quad (6.1)$$

In both simulations, the force felt by the guest is simply  $-\partial U(\mathbf{r}, R_T^{(0)})/\partial \mathbf{r}$  [the temperature dependence of  $W(\mathbf{r})$  is ignored in the adiabatic lattice case and is implicit in the vibrating lattice case]. The result is shown in Figure 7. The data shows that, for the

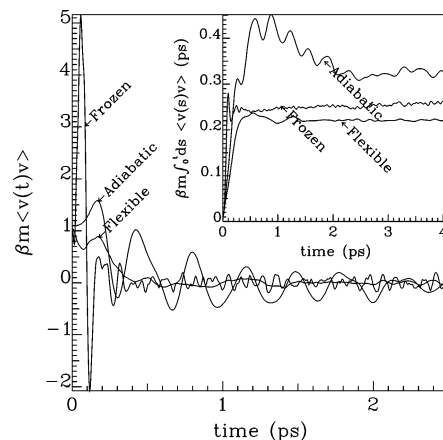


**Figure 7.** Correlation function  $\langle v(t)v \rangle$  and the integral  $\int_0^t ds \langle v(s)v \rangle$ , shown for an argon atom starting at a saddle point in an adiabatic, flexible, and frozen lattice simulation.

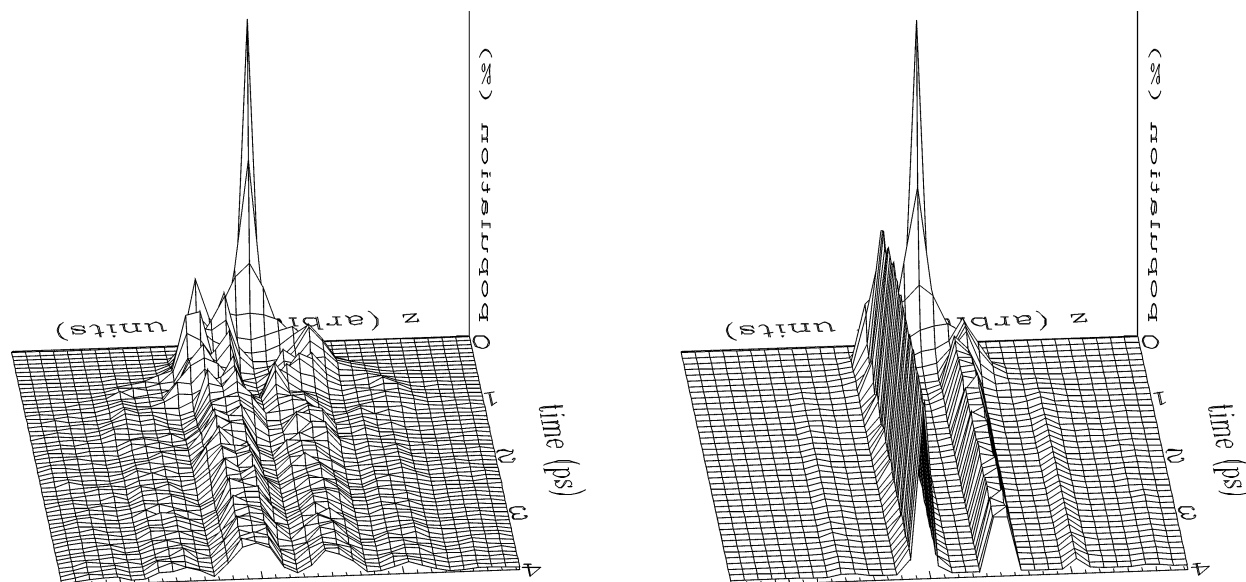


**Figure 8.** Distribution of positions along  $z$  of the 2000 trajectories as a function of time. The left figure is for the adiabatic case, while the right figure is for the unfrozen lattice.

adiabatic lattice, the correlation time is much longer and the integral of  $\langle v(t)v \rangle$  is larger compared with the case where the vibrations are included.

As mentioned in I, there are two mechanisms that contribute to the decay of  $\langle v(t)v \rangle$ . The first is randomization of the velocity directions, while the second is guest energy transfer to and from the lattice vibrations. The results of Figure 7 suggest that, at least for our system, the energy exchange with the lattice is strong enough to shorten the velocity relaxation time, leading to a reduction in the overall diffusion rate. In I, we found the opposite, that is, that this energy exchange time scale was too long and did not contribute strongly to the decay of the velocity correlations.

The behavior of  $\langle v(t)v \rangle$  at short times is very different in the two cases. For the adiabatic case, the guest is initially accelerated down the barrier, producing a peak at short times, while for the real calculation, the collisions with the randomly moving lattice initially slow the guest. In Figure 8, we show the distributions of positions along  $z$  inside the crystal as a function of time. From these figures, it is clear that the trapping of the guest in binding sites is much more efficient for the unfrozen lattice where energy exchange is possible. In the vibrating case, if the guest starts at a saddle point, it travels mainly to the nearest binding sites, and only a small fraction go to second nearest binding sites. It travels farther and with bigger proportion in the adiabatic case.

Also shown in Figure 7 is the velocity autocorrelation obtained from the simulation of the guest released at a saddle point in a completely rigid lattice where the crystal atoms are frozen at their guest-free, equilibrium lattice positions. The short-time behavior shows a much stronger acceleration down the barrier; this is not surprising given the much larger barrier. In addition, we see higher frequency motions, indicative of the rattling motion of the guest in the narrow rigid channel.

In testing the validity of TST, we observed that the temperature dependence predicted by TST is close to the one obtained from our method. The activation entropy,  $\Delta S^\ddagger$ , is also close for the two methods. This is not surprising, since the energy landscape that we have in this system combined with the theory, compare to eq 2.2, gives much more importance to the saddle point region; TST only includes information at the saddle point

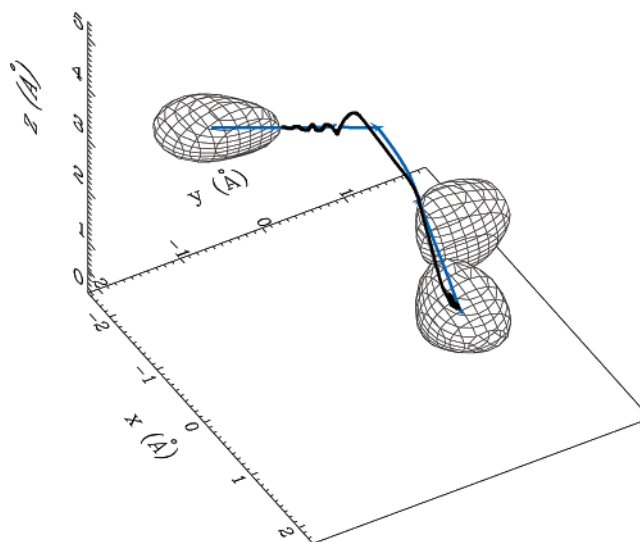


**Figure 9.** Steepest descent path (blue) compared against the average trajectories (black) as obtained from our simulations started at the high-energy saddle point.

[which, of course, is determined from the same free energy surface,  $W(\mathbf{r})$ ].

In Figure 9, we compare the steepest descent path, which is assumed to describe the dynamics in TST, against simulated trajectories that start at the high energy saddle point and that are averaged under the condition that they end up in one of the two binding sites (the black path in Figure 9). From this figure, we conclude that the steepest descent path accurately describes the motion for this system (the oscillations in the black curve are explained by the fact that guest particles with kinetic energy cannot take the sharp turn in the steepest descent path). Note that, starting from the saddle point, 98% of the trajectories end up in one of the two binding sites (almost in a 1:1 ratio). The remainder either get trapped in the local minimum or go to farther binding sites. These observations, combined with the fact that the permeabilities obtained from transition state theory are systematically lower, tells us that something is still missing in TST (note that the TST transmission coefficient, in this case, is close to unity, and in any event, including it would only make the agreement worse). This is surprising since TST usually gives



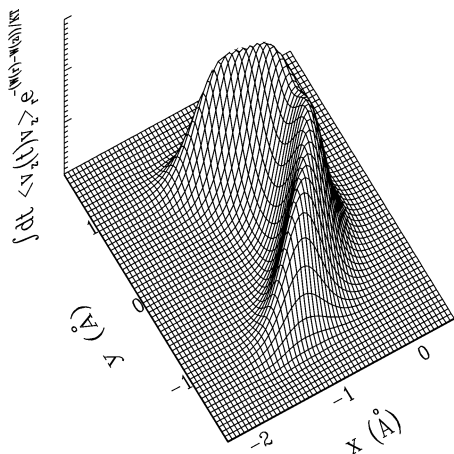


**Figure 10.** Factor  $\int_0^\infty dt \langle v_z(t_1) v_z \rangle_r e^{-\beta[W(r)-W(z)]}$  in the maximum  $W(z)$  plane where an area of  $2.757 \times 3.46 \text{ \AA}$  is shown.

an upper bound to Smoluchowski processes (cf. ref 28). The difference cannot be explained from the cooperative motion of the guest and the lattice atoms since, as shown in Figure 7, the vibrations tend to reduce the diffusion. One possible explanation of the discrepancy between TST and our calculation is the following. First recall that  $D_0$  is obtained from the plane average of  $\int_0^\infty dt \langle v_z(t_1) v_z \rangle_r e^{-\beta[W(r)-W(z)]}$ . This factor is shown in Figure 10 for the  $W(z)$  maximum energy plane (which is very close to the plane that contains the saddle point). In the context of TST, this factor is assumed to be harmonic with the maximum at the saddle point. It is clear from the figure that the harmonic approximation is not accurate. In conclusion, TST seems to more effectively describe the averaged diffusion process in our large energy barriers system ( $18k_B T$  at 300 K) than it did in I for smaller energy barriers ( $2k_B T$  at 300 K), although the assumption about what regions of phase space contribute to the diffusion process is still wrong.

Most experiments (cf. refs 18 and 21) claim that the pre-exponential factor,  $D'$ , as defined in eq 5.7, does not appreciably change with temperature. The prefactor is directly proportional to  $D_0$  and the nonideal corrections appearing in eq 5.4. By assuming the gas is ideal in the bulk and that the saddle-point curvatures are independent of temperature, TST predicts that  $D_0 \propto T^{3/2}$ , compare to eq 4.2. This is not supported by the data, compare to Table 1, since there is significant temperature dependence in the curvatures. Indeed, the TST results are well-described by a  $T^{1.28}$  power law, while our method predicts  $T^{1.1}$ , albeit with larger deviations. In both models, the temperature dependence is clear, but this effect is very hard to see in an Arrhenius plot (cf. Figure 5) and would be even harder to see in a real experiment given the large error bars reported for  $D'$ .

In conclusion, we have shown that the driving forces for the diffusion of a guest in a large energy barrier system are different than in I where we considered a small energy barrier system. The permeability is very sensitive to the accuracy of the activation energy, and that of the underlying potential model, and to the flexibility of the lattice. For a more accurate evaluation of the permeabilities, a potential model that describes the repulsive interactions better, resulting in a more negative activation entropy, would be required. The goal of this work

was to establish what phenomena contribute to the prefactor, and we have shown that the prefactor depends on the cooperative motion between the guest and the lattice. This effect is absent in TST and all frozen lattice or adiabatically equilibrated lattice simulations and can lead to non-negligible errors in systems with large energy barriers and concomitantly large forces.

**Acknowledgment.** First and foremost, we thank the organizers of this *Festschrift* honoring Irwin Oppenheim for inviting us to take part. Irwin has been a mentor and friend for many years, is interested in all aspects of science, and has played an important role in helping many young scientists get started. That he has done all this while, at the same time, remaining a decent and gentle man is something we should all strive to emulate. We thank the McGill's Center for the Physics of Materials for the use of the Beowulf cluster and, in particular, Dr. Juan Gallego for helping us with several parallel processing issues. We also thank the Natural Sciences and Engineering Research Council of Canada for supporting this work. Finally, one of us (B.P.) thanks the *Fonds de recherche sur la nature et les technologies* for support.

## References and Notes

- (1) Palmieri, B.; Ronis, D. *Phys. Rev. E: Stat. Phys., Plasmas, Fluids, Relat. Interdiscip. Top.* **2003**, 68, 046127.
- (2) Vertenstein, M.; Ronis, D. *J. Chem. Phys.* **1986**, 85, 1628.
- (3) Ronis, D.; Bedeaux, B.; Oppenheim, I. *Physica A* **1978**, 90, 487.
- (4) Mehra, V.; Basra, R.; Khanna, M.; Chakravarty, C. *J. Phys. Chem. B* **1999**, 103, 2740.
- (5) Mossell, T.; Schrimpf, G.; Brickmann, J. *J. Phys. Chem. B* **1997**, 101, 9476.
- (6) Mossell, T.; Schrimpf, G.; Brickmann, J. *J. Phys. Chem.* **1996**, 100, 4582.
- (7) Demontis, P.; Stara, G.; Suffritti, G. *B. J. Chem. Phys.* **2004**, 120, 9233.
- (8) Kopelevich, D. I.; Chang, H.-C. *J. Chem. Phys.* **2001**, 114, 3776.
- (9) Demontis, P.; Suffritti, G. B.; Fois, E. S.; Quartieri, S. *J. Phys. Chem.* **1992**, 96, 1482.
- (10) Suffritti, G. B.; Demontis, P.; Ciccotti, G. *J. Chem. Phys.* **2003**, 118, 3439.
- (11) Demontis, P.; Suffritti, G.; Bordiga, S.; Buzzoni, R. *J. Chem. Soc., Faraday Trans.* **1995**, 91, 525.
- (12) Vertenstein, M.; Ronis, D. *J. Chem. Phys.* **1987**, 87, 5457.
- (13) Deutch, J. M.; Silbey, R. *Phys. Rev. A: At., Mol., Opt. Phys.* **1971**, 3, 2049.
- (14) Rickwardt, C.; Nielaba, P.; Müser, M. H.; Binder, K. *Phys. Rev. B: Solid State* **2001**, 63, 045204.
- (15) Schober, H.; Strauch, D.; Nützel, K.; Dorner, B. *J. Phys.: Condens. Matter* **1993**, 5, 6155.
- (16) Striefler, M. E.; Barsch, R. *Phys. Rev. B: Solid State* **1975**, 12, 4553.
- (17) Kloeden, P. E.; Platen, E. *Numerical Solutions of Stochastic Differential Equations*; Springer-Verlag: Berlin, 1994.
- (18) Watson, E. B.; Cherniak, D. J. *Geochim. Cosmochim. Acta* **2003**, 67, 2043.
- (19) Chu, W.-K.; Mayer, J. W.; Nicolet, M.-A. *Backscattering Spectrometry*; Academic Press: New York, 1978.
- (20) Hansen, J. P.; McDonald, I. R. *Theory of simple liquids*; Academic Press: London, 1976.
- (21) Carroll, M. R.; Stolper, E. M. *Geochim. Cosmochim. Acta* **1991**, 55, 211.
- (22) Cherniak, D. J. *Earth Planet. Sci. Lett.* **2003**, 214, 655.
- (23) Béjina, F.; Jaoul, O. *Phys. Earth Planet. Inter.* **1996**, 97, 145.
- (24) London, F. Z. *Phys. Chem. B* **1930**, 11, 222.
- (25) Kirkwood, J. G. *Phys. Z.* **1932**, 33, 57.
- (26) Muller, H. R. *Proc. R. Soc. London, Ser. A* **1936**, 154, 624.
- (27) Barrer, R. M.; Peterson, D. L. *Proc. R. Soc. London, Ser. A* **1964**, 280, 466.
- (28) Chandrasekhar, S. *Rev. Mod. Phys.* **1943**, 15, 1.